Modelling laser modified secondary electron yield response of surfaces

Din, Amin A.; Uren, Robin; Wackerow, Stefan; Fontenla, Ana T. P.; Pfeiffer, Stephan; Tabares, Elisa G.

Published in:
Journal of Physics D: Applied Physics

DOI:
10.1088/1361-6463/ad58ed

Publication date:
2024

OPEN ACCESS
IOP Publishing
Journal of Physics D: Applied Physics
J. Phys. D: Appl. Phys. **57** (2024) 385103 (12pp)
https://doi.org/10.1088/1361-6463/ad58ed

Modelling laser modified secondary electron yield response of surfaces

Amin A Din[1,*], Robin Uren[1], Stefan Wackerow[1], Ana T P Fontenla[2], Stephan Pfeiffer[2], Elisa G Tabares[2], Svetlana Zolotovskaya[1] and Amin Abdolvand[1]

[1] School of Science and Engineering, University of Dundee, Dundee DD1 4HN, United Kingdom
[2] European Organization for Nuclear Research, CERN, 1211 Meyrin, Switzerland

E-mail: adin@dundee.ac.uk

Received 20 March 2024, revised 30 May 2024
Accepted for publication 17 June 2024
Published 27 June 2024

Abstract

Electron clouds hinder the operation of particle accelerators. In the Large Hadron Collider (LHC), the copper beam screens are located within close proximity to the beam path, resulting in beam-induced electron multipacting, which is the main source of electron cloud formation. Conditions for multipacting are encountered when such surfaces have a secondary electron yield (SEY) greater than unity. Roughening the surface through laser processing offers an effective solution for reducing secondary electrons. Laser ablation leaves behind a complex rough, multi-scale geometrical surface with an altered chemical composition. Current models often over-simplify the geometry, do not have sufficient experimental data to derive input parameters, and exclude SEY-reducing mechanisms such as the surface chemistry. Leading to electron-matter interactions which do not resemble that of a real surface. Here, this complex surface is studied on copper used in the LHC, and the influence of microgeometry, inhomogeneous nanostructure and complex surface chemistry on the SEY is investigated. A novel, improved model is proposed that characterises these sophisticated structures, enabling the efficient design of surfaces to reduce SEY. To validate the model, samples were made using a variety of laser parameters. Modelling insights revealed that secondary electron suppression is not only caused by the microgeometry but also the nanostructure and chemical modification play a role. Contrary to the conventional theory, high aspect ratio structures are not necessarily required for effective SEY reduction. Currently, the model is applicable to a variety of surface morphologies and could be employed for other materials.

Supplementary material for this article is available online

Keywords: secondary electron yield, laser materials processing, Monte Carlo methods, nanostructures, multipactor effect, Large Hadron Collider

* Author to whom any correspondence should be addressed.

1. Introduction

Secondary electron yield (SEY) is an emergent property of a material that describes the number of secondary electrons emitted from the material's surface when bombarded by energetic particles, such as primary electrons. Step-by-step, secondary electron emission (SEE) begins with an electron-matter interaction which may induce electron excitations in the solid. The excited electrons then propagate through the material inelastically scattering, those which escape the surface barrier are referred to as secondary electrons [1]. The SEY is a measure of the ratio of the emitted secondary electron current to the primary electron current.

Electron clouds induced by SEE have been detected in particle accelerators for over half a century [2, 3]. In the Large Hadron Collider (LHC), a thin layer of copper is utilised in the beam screen design in order to protect the surrounding superconducting devices and maintain operating conditions by limiting the heat load and grounding the system [4–6]. Although, the beam screens current configuration exposes copper to high-energy protons. Because copper has an innate SEY of approximately 2 (depending on the surface properties), conditions for electron cloud generation become inevitable. Consequently, exceeding the heat load on the system, generating undesired conditions and distorting the beam dynamics thereby limiting the performance of the LHC [3, 7]. With an increase in energy expected from the High-Luminosity upgrade [8, 9], electron cloud formation will be more sensitive to SEE. This makes reducing the SEY of exposed surfaces near to unity more critical.

There are a number of techniques available to reduce the SEY and therefore mitigate electron clouds. All techniques involve either manipulating the surface chemistry and/or inducing surface roughness. Coating a surface with a low SEY material essentially changes the surface's electronic structure and therefore the response to incident electrons. This mechanism is also possible on the nanometre scale and is referred to in the literature as double-layer structures [10–13]. Alternatively, roughening the surface can be used and is capable of both enhancing and suppressing SEE [14]. The former is due to the incident angle-dependent SEY [15, 16]. At grazing incidence, higher energy electrons are able to penetrate the surface within the electron escape depth [17]. Therefore interacting with more internal electrons, while preventing significant inelastic events on their transport through the solid, thus emitting more secondary electrons. The latter is applicable to highly rough surfaces and is characterised by the secondary electron's ability to escape the rough structure. On increasing roughness, the probability of inelastic events is increased, therefore reducing SEE due to the low-energy SEY being less than unity.

In the literature SEY reduction techniques vary from coating the surface with a low SEY material [18, 19], inducing surface chemistry changes via conditioning/heating [20, 21], texturing the surface through a variety of techniques such as laser processing [22–25]/depositing a porous coating [26] or a combination of these techniques [27].

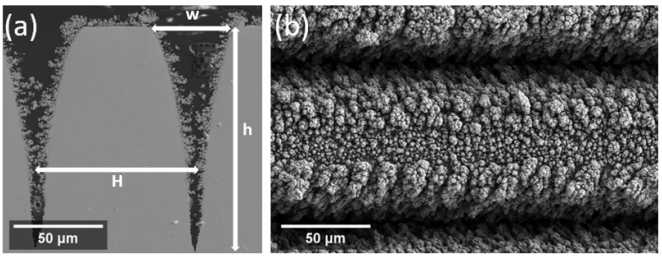

Figure 1. Scanning electron microscopy (SEM) images of LESS produced by a solid-state laser operating at 532 nm with a pulse duration of 10 ps, with an aspect ratio, ($A = h/w$), of 2.4 and a porosity, ($P = w/H$), of 57%, (a) side view, (b) top view illustrating redeposited compact and dense cauliflower structures.

For the copper beam screens reducing the SEY $in-situ$ is desired, for which laser engineered surface structuring (LESS) is considered an effective method [23, 28]. LESS is where a pulsed laser source is used in order to write highly organised structures onto a surface. A by-product of the laser structuring is the re-deposition of the removed material on the surface in the form of nanostructures and an altered surface chemical composition [29–35]. Figure 1 illustrates an example of LESS produced by a solid-state laser operating at 532 nm with a pulse duration of 10 ps. These structures are obtained by controlling laser parameters to tailor their geometry, which includes the microgeometry and nanostructure. The microgeometry is described by the aspect ratio and porosity. The nanostructure observed is characterised by its size, shape and porosity. There are generally three types of nanostructures observed associated with LESS [36], compact and dense cauliflower structures, less compact structures and laser-induced periodic surface structures (LIPSS) [37].

In order to optimise laser structuring for SEE reduction in a variety of materials and applications, it is requisite to understanding the mechanisms responsible for reducing SEE and shifting the maximum SEY. Currently, there are limited specific studies in the literature modelling precisely LESS while capturing this SEY-energy dependence [38].

Meeting the SEY specifications of any device, in this case, the LHC, can be an engineering challenge requiring many experimental iterations, thus consuming both time and resources. If the mechanisms responsible for SEY reduction are understood via predictive modelling, surfaces can be technically designed to meet requirements.

There are several models in the literature which have the ability to approximate the SEY of porous structures [39–44]. Although current models often over-simplify the geometry, do not have sufficient experimental data to derive input parameters, are limited to multiple electron generations and exclude critical SEY-reducing mechanisms such as the modified surface chemistry (figure 2 illustrates the surface chemistry post-LESS on our copper) which therefore leads to electron-matter interactions which do not resemble that of a real surface. This could be due to the challenges involved in modelling the nanostructure, in addition to quantifying and measuring

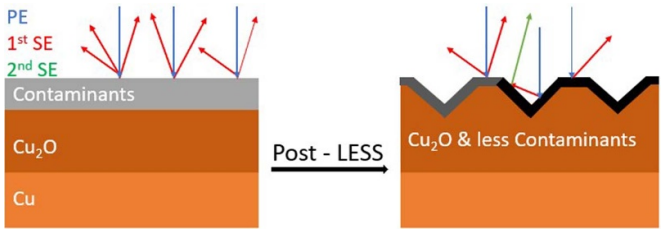

Figure 2. Simplified SEY reduction theory of LESS treatment in nitrogen atmosphere, example with two different nanostructures deposited. Dark grey: less compact structures. Black: compact and dense cauliflower structures.

the SEY and SEY-related properties (incident angle dependence and SEY-energy spectrum) of a poorly defined surface composition post-processing, especially if there is nanostructure involved. Since it becomes very difficult to disentangle the nanostructure from the surface chemistry and understand to what extent the nanostructure alone would affect the SEY. Considering only the microgeometry, previous models are acceptable. However when modelling LESS, to capture the energy-dependent electron response, one needs to consider the inherent SEY-energy spectrum, incident angle-dependent SEY, complex nanostructure and the variation in surface chemistry due to the formation of such nanostructures.

Through simulation, the objective here is to reveal the mechanisms responsible for suppressing SEE in LESS, understand why the SEY-energy dependency changes and ultimately provide a predictive model which could offer insight into the design of surfaces for meeting technical specifications.

2. Methods

2.1. Furman's model

The working principles of the phenomenological model are detailed by Furman *et al* [45] and will briefly be covered here. The model input parameters are obtained by fitting experimental SEY data of the desired untreated surface, in this case, multiple forms of copper (refer to appendix A.1 for more details). Using this information, the probability description of SEE can be determined on a single electron-matter interaction basis. Therefore, adjusting the geometry and surface conditions within CST Studio Suite facilitates the simulation of technical surfaces.

Table 1 illustrates some of the parameters used to fit SEY data (see supplementary material) corresponding to our recently measured as-received copper at CERN (from hereon will be referred to as AR), cuprous oxide (Cu_2O) and amorphous carbon (a-C). [20, 36] The AR copper state is not a well-defined state and the SEY can vary depending on the level of contamination [46, 47], in the literature values range from $1.9-2.2$ are given [20, 22]. These parameters are then inputted into probabilistic density functions in order to determine the number of secondary electrons emitted, their

Table 1. Partial overview of model fitting parameters.

	Elastic Parameters (δ_e)							
	E_e' (eV)	$P_{1,e}'$	σ_e	$P_{1,e}$	W (eV)	p_e	e_1	e_2
Cu AR	0	0.23	1	0.01	220	1	2.1	2.1
Cu_2O	0	0.26	1	0.02	130	1	1.8	1.6
a-C	0	0.17	1	0.01	200	1	0.9	0.9
	Inelastic Parameters (δ_r)							
	E_r (eV)	$P_{1,r}$	r	q	r_1	r_2		
Cu AR	40	0.45	1.45	0.4	0.01	0.0		
Cu_2O	150	0.58	1.45	0.4	0.01	1.0		
a-C	200	0.20	1.60	0.4	1.20	1.2		
	True Secondaries Parameters (δ_{ts})							
	$E_{ts,\max}$ (eV)	$\delta_{ts,\max}$	s	t_1	t_2	t_3	t_4	
Cu AR	300	1.46	1.57	1.05	0.95	1.15	1.0	
Cu_2O	425	0.83	1.58	1.23	1.10	1.15	1.1	
a-C	240	0.74	1.75	0.73	0.93	0.70	0.6	

angles, and energies when a primary electron with incident energy and angle collides with the surface. In this model, the angular-dependent SEY is proportional to $[1+e_1(1-\cos^{e_2}\theta)]$, where e_1 and e_2 depend on the surface state. The scaling variables are determined through recent SEY measurements of sputter-cleaned copper up to 50^0 incidence, illustrated in the supplementary material, and we assume that all emitted electrons follow a cosine angular distribution regardless of their energy. The emitted secondary electrons' energies are characterised by experimental SEY-energy spectrum data [48]. Then a particle tracking solver is used to record electron trajectories and the process is repeated on successive electron-matter interactions. The employed Monte Carlo method results in SEY behaviour converging towards the inputted untreated surface. To realistically model electron-matter interactions, emitted secondary electrons are segregated based on their energy and are parameterised. Elastic electrons of energies E_oeV are electrons emitted with little or no energy loss. True secondary electrons are conventionally described as electrons with energies below 50 eV. Finally, inelastic electrons are those with energies in between the true and elastic boundaries. The tabulated parameters characterise the SEY-energy relationship of each type of secondary electron and the angular dependence. δ_e, δ_r and δ_{ts} are calculated according to equations (A1)–(A3). The SEY fit of the inputted flat surface (δ_f) is the sum of each type of emitted electron (equation (1)), plotted in the supplementary material

$$\delta_f = \delta_e + \delta_r + \delta_{ts}. \tag{1}$$

2.2. LESS modelling

We considered a trench-like geometry, illustrated in figure 3, induced by LESS, that is finite in the x-axis and periodic in

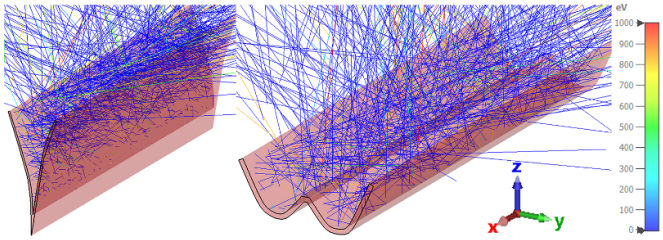

Figure 3. Cross sections of LESS geometries bombarded by 1keV primary electrons at $t = 0.4$ ns in CST Particle Studio. Left presents a trench with an aspect ratio, $A = 2.05$ and the right, $A = 0.41$. only SEs are shown at reduced density to clearly illustrate inelastic scattering.

the y-axis. In order to reproduce the actual conditions of LESS accurately and concisely, a number of assumptions were introduced. First, it is assumed that the geometry is homogeneous, and therefore a section of interest can be extracted which on average represents the entire surface. In this case, the trench is modelled and the surrounding untreated region is factored in depending on the porosity (illustrated in figure 1), thus constituting a unit cell. To consider the finite structure in the x-axis, reflecting surfaces with a SEY of unity confine the electrons to the geometry. In this case the reflecting surfaces have a cosine angular distribution and therefore the length of the structure needs to be significantly larger than the height of the trench in order to limit the number of electrons interacting with these surfaces. To reflect LESS conditions and better model electron-matter interactions, the microgeometry was obtained by sketching over cross-sections of the sample's trench. Care needs to be taken when modelling large aspect ratio trenches since the nanostructure could fill the trenches, reducing the depth the electrons can interact with.

Regarding the nanostructure, this was slightly more complicated to model precisely due to its inhomogeneous distribution, density, arbitrary shapes and sizes as well as the multiple scales of geometry present. A similar approach was taken to model the nanostructure, i.e. taking a small nanostructured section from SEM images, illustrated in figure 4. By thresholding the pixels of the SEM image, the area coverage of nanostructures was extracted and the porosity was determined. The nanostructure's height was approximated based on cross-sections and was assumed to have an aspect ratio close to unity. The surface area of the nanostructures was approximated by sketching their profile. Finally, the 3D geometries were visually modelled based on this information to better resemble their electron response. To simplify the variance in nanostructures among different samples, three types of nanostructures were simulated in order to determine their secondary electron-trapping capabilities, illustrated in figures 4 and 5. Firstly, compact cauliflower structures (denoted H), which have an agglomerate form causing a high porosity and aspect ratio [33], suggesting a greater trapping effect. Secondly, non-compact structures (M), having a slightly lower aspect ratio implying a reduced trapping potential. Finally, less dense LIPSS (L), which have little to no reduction factor as inferred by the literature [49, 50], due to their limited aspect ratio and therefore trapping ability as well as the less modified surface and therefore increased contaminants. Ultimately the role of the nanostructure in electron-matter interactions in LESS: increases grazing incidence and therefore SEY, reduces the secondary electron's escape probability within the trench due to emission angles less likely to meet the conditions for escaping, inducing successive collisions with other nanostructure (resembling microgeometry suppression technique) dampening the emitted electron's energy within the trench and coating the surface with a potentially modified composition and therefore SEY-energy relationship. Therefore, the exact shape of the nanostructure can be approximated provided the conditions simulated are close to what the incident electron on average sees, i.e. more protrusions than normal incidence and the size and porosity are within reason.

Through SEM observation, the presence of nanostructures both within and between the trenches on the surface post-laser ablation indicates that the nanostructure globally modifies the SEY. It is important to note that some trenches have different nanostructures within and between the trenches.

Since laser ablation induces chemical modifications on the surface this will need to be accounted for in the model. The accumulated fluence irradiated on copper can be categorised and calculated according to Bez *et al* [34] For low fluences < 100 J cm^{-2}), the surface becomes Cu_2O dominated, a gradual increase in the fluence results in the coexistence of Cu_2O and CuO, and finally a further increase leads to the prevalence of CuO. However, surface contaminants will likely still be present which will result in local areas with different SEE behaviour. Therefore to simplify this complex surface dependence, here we assume that for a fluence beyond 1500 J cm^{-2} the probabilities of SEE can be derived from CuO and for a reduced fluence, provided sufficient material is removed and the untreated region is coated in nanostructures, the surface can be characterised by Cu_2O. If a nitrogen-rich atmosphere is used during laser processing, we can assume the surface is likely dominated by Cu_2O. As in the literature, it is observed that nitrogen suppresses further oxidation and the nanoparticles become passivated. [51] Although, if the surface is not coated in nanostructure or there are LIPSS present, the SEE probabilities can be derived from AR copper. This assumption facilitates electron-matter interactions which resemble the actual post-processed surface.

Once the geometrical conditions were defined, the materials were assigned, and a tetrahedral mesh was applied. Next, the electron-emitting surface was calibrated to emit $\geqslant 1 \times 10^4$ electrons. Lastly, the model was set to iterate through incident electron energies between 50 eV and 1000 eV. This is the range of interest in the LHC which determines multipacting.

The extracted results from the model include the incident and emitted currents which can be segregated into nth generations of electrons, average energies of nth generation of secondaries as well as the number of collisions. Secondary electrons are recorded up to the 8th generation. Beyond this, the average secondary electron energies drop below 20eV and no longer significantly contribute to the SEY. The cutoff point of 20 eV is somewhat arbitrary and was chosen because the

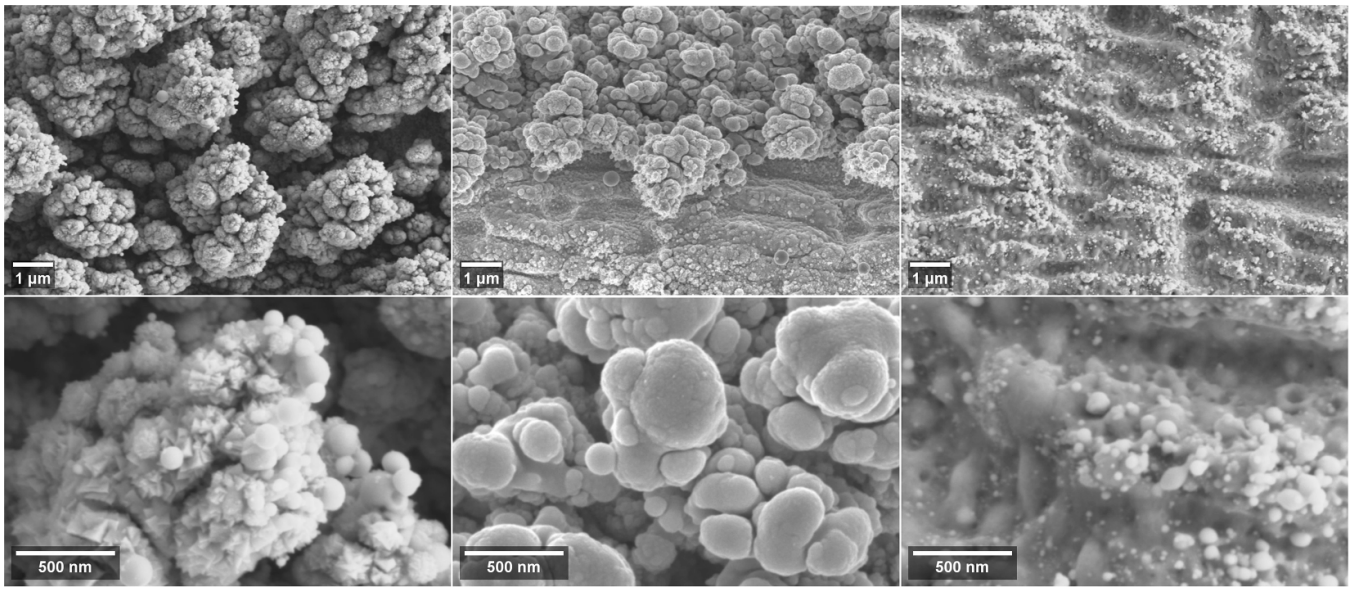

Figure 4. SEM micrographs of the three common nanostructures observed on the untreated area after ablating copper with a solid-state laser operating at 1030 nm with a pulse duration of 800fs; compact cauliflower clusters, non-compact molten structures and LIPSS, respectively. Top row at 10 000 × and the bottom at 50 000 × magnification. These three structures can vary in size, shape, distribution and density. Though one could assume on average, over a macro-region, their properties are homogeneous.

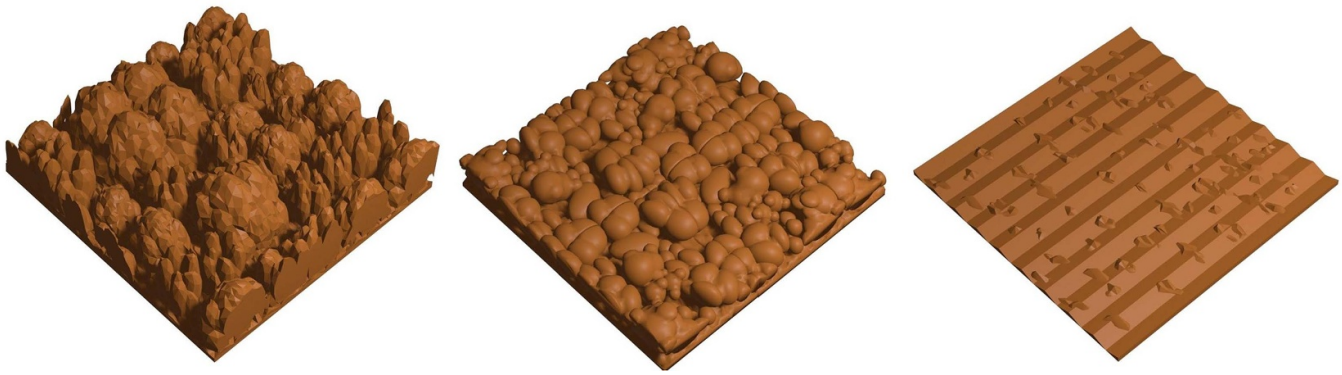

Figure 5. Left, middle and right images present a 20% porous cauliflower structure (H), a 10% porous less compact structure (M) and a LIPSS (L) with an aspect ratio of 0.24 and a period of 350 nm, with an average incidence of 57°, 41° and 27° respectively. Note, the H structure is validated through a-c simulations (mentioned later in the text). Structure details were decimated for reasonable computing speeds.

probability of generating further electrons beyond this energy is almost negligible for copper.

From the extracted collision and emission current data, I_c, I_e, the sample, primary and secondary currents, I_s, I_p, I_{sec} are:

$$I_s = I_c - I_e \tag{2a}$$

$$I_{sec} = I_p - I_s. \tag{2b}$$

Now the SEY of LESS can then be determined. Firstly, the nanostructure between the trenches is modelled and assigned a material according to the accumulated fluence and ambient treatment conditions. Then the nanostructure is simulated at 0° and 50° incidence and the SEY is calculated to obtain its angle-incident SEY behaviour

$$\delta(ns_t) = \frac{I_{sec}(ns_t)}{I_p(ns_t)}. \tag{3}$$

The extracted SEY data of the nanostructure deposited within the trench, $\delta(ns_t)$, is then fitted and a new material is defined which generates SEE probabilities that resemble the nanostructure's electron-matter response. Next, the trench geometry, $\delta(t)$, is simulated using this SEY behaviour, therefore holistically including the geometrical and chemical SEY dependents

$$\delta(t) = \frac{I_{sec}(t)}{I_p(t)}. \tag{4}$$

Then the untreated region's nanostructure, $\delta(ns_{ut})$, is simulated

$$\delta\left(ns_{ut}\right) = \frac{I_{\text{sec}}\left(ns_{ut}\right)}{I_{\text{p}}\left(ns_{ut}\right)}. \tag{5}$$

Finally, the SEY of LESS, δ_{LESS}, is calculated, where P is the porosity, illustrated in figure 1

$$\delta_{\text{LESS}} = \delta\left(t\right) \times P + \delta\left(ns_{ut}\right) \times \left(1 - P\right). \tag{6}$$

2.3. Experimental methods

Several samples were produced using different laser parameters (see appendix B, table 3) in order to validate the model and develop a greater understanding of the relationship between LESS and SEY. Here, four sample sets will be introduced, green series (G), delta series (D), infrared series (IR), and finally diffractive optical element series (DOE). Each series intends to offer a unique insight into the role of laser-structuring on SEY. The first three sets involve the typical u-shaped trenches. The green series investigates the change in aspect ratio on SEY. The IR series focuses on generating different nanofeatures. The delta series is included as our group has done some further experimental studies using this parameter set, specifically, coating these structures [27], eliminating the complex surface chemistry entangled with the nanostructure formation. Thus enabling the investigation solely into the role of micro- and nanofeatures on the SEY and validating the H-type nanostructure. This is possible by simulating the trench microgeometry with a modelled cauliflower cluster and then slightly modifying the modelled cauliflower cluster to better fit the SEY behaviour. Since Pivi *et al* [39] has demonstrated that modelling simple microstructures can give a good SEY prediction. Finally, the DOE set is unique because the beam shaping through the DOE distorts the power distribution generating w-shaped trenches which have never been modelled before. Therefore, each sample will have some degree of variation; whether that is microgeometry, nanostructure or surface chemistry. Providing the opportunity to study each SEY-reducing mechanism and its influence on the SEY and validate the model.

We describe the experimental procedure involved in making sample set G [22], which is the same for the D series, which are then coated according to Himmerlich *et al* [27] Refer to our previous work [49] for the parameters for producing the DOE set. The IR series experimental procedure is the same as the DOE series setup however the DOE is removed as well as using different parameters.

Once the samples were produced, various techniques were used to characterise the samples. SEY data was measured on each sample using the collector method at CERN, see supplementary material, with further details elsewhere [52]. In order to model the samples, for the microgeometry, the trench cross-sections and nanostructure SEM images were collected according to Bajek *et al* [22], and XPS data was recorded following the procedure reported by Bez *et al* [34] For deriving modelling parameters untreated samples were characterised, SEY data was collected for AR copper, Cu_2O and CuO, sputter-cleaned copper and amorphous carbon. As well as SEY-energy spectrum data for AR copper, sputter-cleaned copper and amorphous carbon according to Schulte *et al* [48] Lastly, angle-dependent SEY data was collected for sputter-cleaned copper.

3. Results and Model Validation

3.1. Experimental Comparison

The sample characteristics and results are summarised in table 2. Figure 6 presents a comparison between the experimentally measured SEY (blue) and the proposed model (red). The proposed model is capable of reproducing electron-matter interactions in LESS. The model's predictive ability is attributed to the better-approximated microgeometry, the inclusion of the nanostructure and surface composition. As well as accurate SEY experimental characterisation which enables realistic probabilities of SEE and associated energies. Therefore, simulated electron-matter interactions better resemble that of a real post-processed surface. The reason for this, if we consider the complex surface left behind after laser ablation, there is a multiscale geometry that includes a trench with a number of smaller protruding features as illustrated in figure 7. Furthermore, due to the light–matter interaction inducing extremely high temperatures on the surface and the environmental conditions of processing, the surface composition will inevitably change [29–31, 33–35].

When an electron collides with such a surface, due to the surface morphology there is an increased probability of the electron interacting at grazing incidence (therefore accurate SEY-angle-dependence data is required). Upon the electron's transport through the solid, the energy loss mechanisms, density of states and work function are no longer that of the AR copper state, but now tending towards a more oxidised copper with less contaminants as discovered through XPS data. Therefore, this electron is no longer exciting as many internal secondaries as before and thus fewer electrons are being emitted into vacuum, thereby reducing the SEY (thus the surface chemistry needs to be characterised for accurate SEE probabilities). Not only this, the electrons that are emitted from the surface now have to escape the LESS. These electrons, depending on the surface structures, may encounter vast amounts of nanostructures that inelastically scatter incoming electrons thereby reducing their escape probability and reducing the SEY due to successive low-energy electron-matter interactions. Therefore, to reproduce electron-LESS interactions, a good approximation of the surface structures and SEE energies are important ingredients in obtaining the correct SEY. Again, the electrons that escape the nanostructures need to be within the escape angle of the trench in order to be emitted into free space and contribute to beam-induced electron multipacting. Otherwise these mechanisms will continue to occur, suppressing a number of emitted secondary electrons.

Table 2. Sample properties.

Sample	Cu AR	*G*1	*G*2	*G*3	*D*7	IR1	IR2	DOE1	DOE2	DOE3
Aspect Ratio	—	2.05	1.10	0.50	0.80	0.68	0.53	0.41	0.71	0.20
Porosity	—	0.57	0.57	0.57	0.85	0.76	0.76	0.79	0.60	0.61
ns_t	—	H	H	H	H	H	H	H	H	M
ns_{ut}	—	H	H	M	H	M	L	H	M	H
Cu (in at. %)	24.3	47.1	—	—	—	—	—	33.9	26	27.7
C (in at. %)	40.6	12.9	—	—	—	—	—	30.1	42.5	45.1
O (in at. %)	32.0	40.0	—	—	—	—	—	30.8	26.7	27.2
N (in at. %)	1.9	—	—	—	—	—	—	5.2	4.9	—
δ_{max}	1.99	0.90	0.98	1.16	0.86	1.14	1.30	1.00	1.23	1.56
δ_{max} Model	1.98	0.78	0.86	1.24	0.90	1.09	1.32	1.07	1.11	1.31
E_{max} (eV)	300	750	750	650	780	650	450	600	500	450

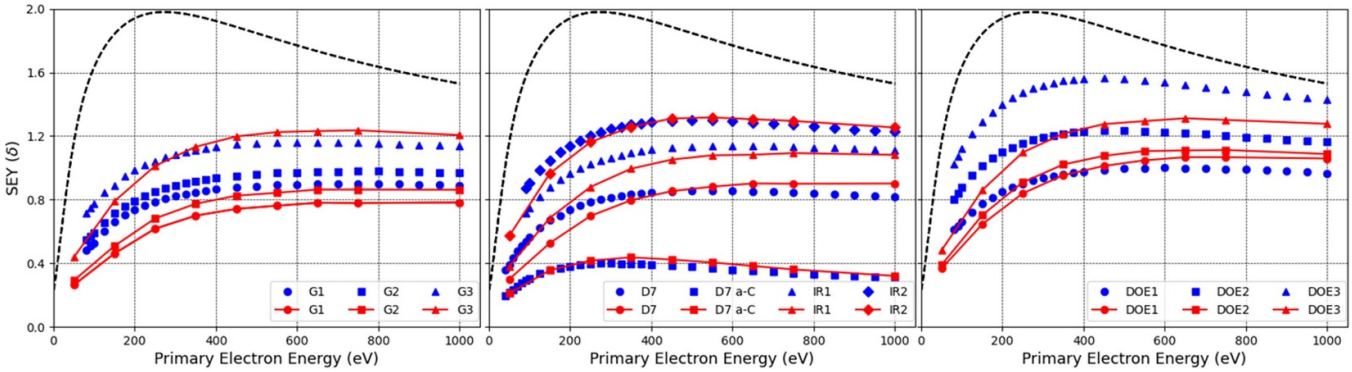

Figure 6. SEY data, the dashed line represents air-exposed copper (AR state), blue is experimentally measured and red is LESS modelled.

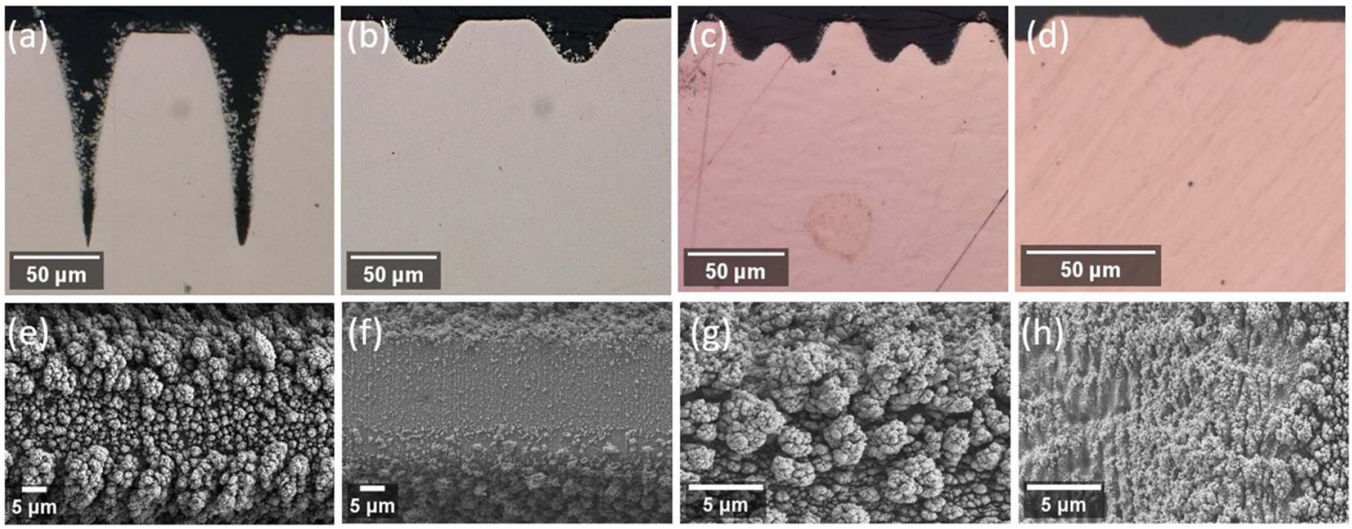

Figure 7. Cross-sections and SEM images of the untreated surface from LESS samples. (a), (e) *G*1, (b), (f) *G*3, (c), (g) DOE1, (d), (h) DOE3. Himmerlich *et al* [27] presents images of sample *D*7 before and after coating.

Therefore, models which oversimplify the multiscale geometries, exclude the post-processed chemical modifications and have insufficient experimental SEY data are not appropriate for LESS, and will lack the ability to capture the SEY-energy relationship. A maximum error in δ_{max} of 20% has been observed despite a variety of geometrical and surface chemistry dependents, thereby validating the model.

3.2. Model insights

Through modelling LESS it is realised that the idea of a high aspect ratio structure is not a requisite for SEY reduction, even in the case where a less compact nanostructure is deposited (table 2, samples *G*3, IR1, IR2, DOE2 and DOE3). Trenches of insignificant aspect ratio (< 1, depending on the lateral wall

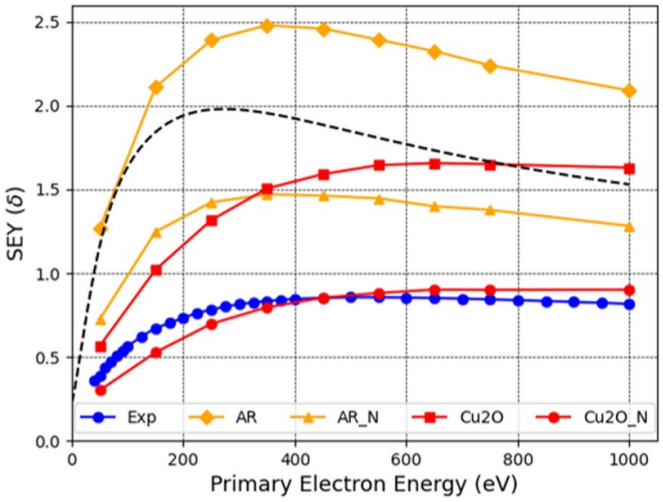

Figure 8. Simulated SEY of sample *D*7, excluding SEY reducing mechanisms such as chemical and/or nanofeature contributions. Exp refers to the measured SEY. AR simulates a unit cell covered in AR copper, excluding nanofeatures. AR_N is the same but includes the nanofeatures. Cu_2O simulates a unit cell coated in Cu_2O, excluding nanofeatures. Finally, Cu_2O_N holistically includes each mechanism.

angle) on an AR copper surface do not suppress SEE effectively, in some cases they may enhance it. This is due to the grazing angle incidence phenomenon [15, 16], the low first cross-over energy and the large escape probability of the low aspect ratio trench [44]. To illustrate this, let us consider the *D*7 sample with an aspect ratio of 0.8 and a porosity of 85%. Simulations were conducted for changing the SEY-reducing variables such as the surface chemistry and nanofeatures. In figure 8, sample AR represents a simulation of the micro-geometry feature on sample *D*7 characterised by AR copper, excluding the nanostructure contribution. Clearly, the SEY globally increases. Upon including the nanofeatures, sample AR_N, SEY reduction becomes possible although not to the extent measured experimentally. Again if we exclude the nanofeatures and conisder a Cu_2O dominated surface the SEY with respect to air-exposed copper is lower, although again does not resemble the experimental data. Once both mechanisms are included, i.e. both surface chemistry and nanofeatures, Cu_2O_N, we see a better prediction of the SEY. Thus this engineered surface reduces the SEY through nanofeatures and the oxidised surface (with reduced contaminants present), facilitating geometrical trapping.

If geometrical features are fabricated in such a way that the surface composition changes, which LESS does based on the XPS data (table 2) and the literature [27, 34, 51], the SEY will also change. Upon laser processing, a transition from contaminated air-exposed copper to a less contaminated cuprous/cupric oxide will reduce the SEY regardless of geometrical effects [17, 34]. This is because the incident electrons now interact with a more oxidised surface which has a lower SEY [14, 20] compared to a collision with an air-exposed surface [13, 27, 46, 53]. However, the extent of this reduction is difficult to quantify due to the undefined contaminated states of AR copper and therefore the compositional changes post-LESS will vary making it challenging to model. It is important to note that the surface composition's SEY reduction capabilities will differ depending on the material and initial surface state.

The role of geometry, specifically nanostructures was investigated in order to observe their effect on SEY. Simulations suggest that geometrical trapping is a present suppression mechanism for cauliflower and non-compact features whereas for LIPSS it is likely chemistry dominant. It is clear that nanofeatures are capable of lowering the SEY, although their ability is dependent on the type of nanostructures deposited and the material. For example, the same cauliflower nanostructure could behave very differently if coated in alumina as opposed to copper. Since alumina's high SEY and low first cross-over energy [54] makes the surface behave like an electron multiplier compared to the desired suppressing effect observed on copper. The same structure could also behave differently on a low SEY material such as amorphous carbon. In this case it will be more suppressive compared to copper due to the increased probability of absorption for low-energy electrons and reduced inelastic coefficient. Therefore, to conclude there is a range of potential SEY reduction which the nanostructures (geometrical features) can offer.

Modelling LESS indicates the shift in δ_{max} to higher energies is a function of the incident angle-dependent SEY, inelastic electron yield, and surface chemistry. The angle-dependent SEY increases SEE for higher energy electrons and it is evident that a shift is observed solely due to the angle-dependence [55]. Additionally, a high inelastic electron yield, δ_r, (see figure 9, in the case of energetic incidence where the backscattered electron yield dominates) will increase the number of inelastic events a secondary electron can undergo within the rough geometry. Multiplying the next generation of SEE further, providing electrons with an increased escape probability, favouring energetic incidence. Another influencing mechanism could be the emission angle of the δ_e and δ_r contributions of secondary electrons which are assumed to follow a cosine distribution rather than their actual lobe-like angular distribution [56]. On the other hand, surface chemistry may increase the first cross-over energy and therefore increase the probability of low-energy electron absorption [57]. Each mechanism combined manipulates the SEY-energy relationship, generally shifting the maximum SEY to a higher energy. Considering the D7 sample, insights into the SEY-energy shift can be offered. Post laser treatment, the SEY is reduced and the typical shift in δ_{max} is observed. Simply coating the sample in amorphous carbon reduces the plateauing behaviour, despite maintaining a rough structured surface, which is associated with a shift in δ_{max}. This is attributed to high first crossover energy and the low inelastic coefficient of amorphous carbon [48]. The δ_r component for an untreated surface beyond δ_{max} is below 0.2 for amorphous carbon compared to a δ_r of between

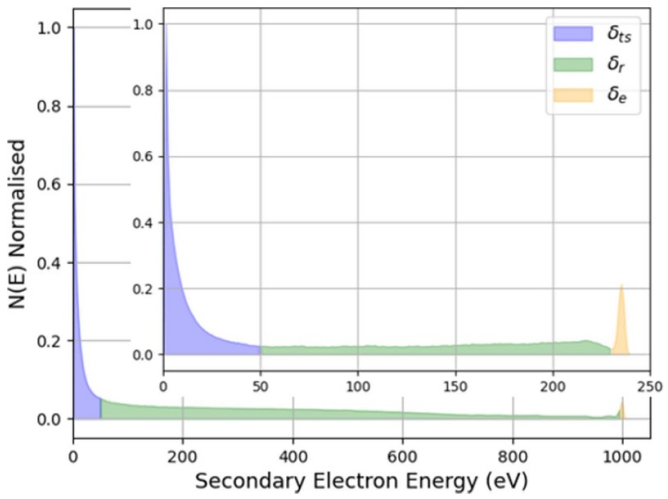

Figure 9. Measured energy distribution curve, N(E), of Cu AR [48], segregating secondary electrons according to their energy.

$0.5-1$ for copper. Therefore, when an electron of 1000 eV interacts with amorphous carbon, on average on average secondaries will exhibit energies below 50 eV. Whereas for copper a larger number of secondaries will have energies beyond 50 eV. Thereby increasing the SEY, causing a more significant shift. A marginal shift is still present however this is solely from the incident angle-dependent SEY.

3.3. Modelling performance and LESS design for SEY

The model performance is consistent, although the surface chemistry assumption can lead to increased error margins, since in reality, the surface composition will never be constant. There are few conditions that may arise, for example, not considering any surface adsorbates, since these species will always be present. Although, the model remains accurate despite this assumption. Possibly because the modelled nanostructure is less suppressive than its real counterpart. As opposed to the surface composition, creating a balance. Ultimately culminating in a relatively accurate description of a laser-treated surface. Consequently, this is likely the reason for underestimating the low-energy SEY. Another possible error may arise if samples are treated in air at a moderate fluence. Since a coexistence phase of Cu_2O to CuO emerges making it challenging to characterise the surface composition. Furthermore, an increased error margin may be expected when insignificant material is removed and the surface left behind is in a copper state similar to its AR state but with reduced contaminants, which can be observed in sample DOE3. Considering the DOE sample set (figures 7(c) and (d)), comparing DOE1 to DOE3, the aspect ratio in both cases is insignificant to reduce the SEY of AR copper. The reason why DOE1 is a better secondary electron suppressor is because of the higher laser power and reduced hatch distance causing more removed material implying a less contaminated surface. Furthermore, within the trench, DOE1 is coated in a cauliflower structure which facilitates electron trapping compared to DOE3 with a smaller aspect ratio with less compact and LIPSS features present in the trench (figures 7(g) and (h)) which would likely resemble a more contaminated surface and therefore higher SEY.

Modelling error is inevitable and will arise due to the sophisticated surfaces. Other possible modelling discrepancies may stem from deriving angle-dependence parameters of each material from clean copper, underestimating the angle-dependent SEY beyond 50^o, using a cosine angular distribution for all emitted electrons and simplifying the nanofeatures down to three types of structures.

One needs to be careful when modelling higher aspect ratio structures. From figure 7, upon increasing material removal with a gaussian beam, the u-shaped trenches become relatively narrower. This may result in the bottom of the trench being clogged up with nanostructure, thus not actually reflecting a trench of such aspect ratio which could result in an inaccurate calculated SEY. This could explain the SEY plateau upon increasing ablation depth observed by Bez *et al* [34]

Although, this is not important as the model offers crucial insight into the electron response of technical surfaces and assists with the design and optimisation of highly organised surface structuring. Also, for implementing LESS, high aspect ratios may not meet environmental constraints and inhibit system performance.

It is possible to forecast the SEY of LESS using this model as well as LESS covered in coatings. In order to do so, the surface needs to be sufficiently characterised. The microgeometry cross-sections and SEM images of the nanostructure are mandatory for deriving and selecting the simulation geometries. Sufficient experimental data such as the post-processed surface composition and corresponding SEY behaviour are necessary in order to obtain realistic input parameters. As of now, the proposed model has been applied to a variety of materials such as copper and amorphous carbon, it is appropriate for any material provided its SEY and post-processing surface properties are known.

Currently, Furman's model has a possible limiting assumption (equation (39) described by Furman and Pivi [45]) where if a primary electron induces the emission of multiple secondaries their energies have to be less than 50 eV which experimentally may not be true. Making it difficult to accurately fit some higher SEY materials such as AR Copper. This assumption needs to be addressed in order to realistically simulate high SEY materials.

Finally, modelling suggests that two key variables influence the mechanisms responsible for SEY reduction; the damage threshold and hatch distance. Since the higher above the damage threshold one processes, the more material removed, a greater increase in the modification of the surface composition and a resultant dense nanostructure deposited globally, if combined with a hatch distance similar to the beam size [34, 36]. These variables are capable of manipulating each mechanism's

role in SEY reduction of LESS. Though other variables such as the beam size and scan speed can achieve a similar effect. Which variable to manipulate will depend on the material, application, and processing setup. For instance, in some insulators like alumina, geometrical features alone may not always reduce the SEY. Therefore, selecting laser parameters that globally modify the surface composition in tandem with a suitable geometry can lead to effective SEE suppression. Another example, more relevant could be a situation where depth is a constraint, thus limiting the aspect ratio of structures. In this scenario, opting for a hatch distance slightly smaller than the beam size with a relatively high multiple above the damage threshold will permit effective SEY reduction due to the formation of nanostructure and the modified surface composition. However, for applications requiring structuring to be conducted in a tight timeframe, non-overlapping trenches with low aspect ratios can sometimes meet the specifications. Since the deposited nanostructure can sometimes indirectly modify the surface chemistry assisting in SEY reduction. Additionally, depending on the application and material, controlling the ambient gas conditions could assist with SEY reduction and possibly improve the post-processed material properties.

4. Conclusion

The mechanisms responsible for SEE and SEY reduction upon laser surface modification are revealed through simulation and validated experimentally. The proposed model is capable of capturing the SEY-energy relationship as well as accurately determining the maximum SEY of a given treated copper surface. By computationally reproducing surfaces similar to LESS and deriving input parameters from experimental data, realistic probabilities of SEE and associated energies were realised, facilitating LESS modelling. Contrary to the conventional theory, high aspect ratio structures are not necessarily required for effective SEY reduction. This can be achieved by selecting suitable lasing parameters.

Data availability statement

All data that support the findings of this study are included within the article (and any supplementary files).

Acknowledgments

The authors would like to express their gratitude towards CERN specifically; D A Zanin and M Rimoldi for supplying SEY measurements presented in figure 6, M Himmerlich, V Petit and M Taborelli for collecting SEY and SEY-related data (presented in supplementary material section) enabling the derivation of input parameters and for fruitful discussions, and the Science and Technology Facilities Council (STFC) of the United Kingdom for their support through Grant: ST/T001887/1.

Appendix A. Model input parameters

A.1. Furman's model

The following parameters are used to fit the untreated surfaces' SEY data. These values are obtained from theoretical fits, extrapolating experimental data and measuring the SEY and SEY-energy spectrum. For predictive results, accurate experimental data is critical.

Below defines the elastic, inelastic and true SEY-energy relationship, these values are obtained by integrating the SEY-energy spectrum. For example, if the measured energy spectrum for an incident electron is 40eV, one can integrate between $0-20$ eV to obtain the true SEY contribution, $20-(E_0-5)$eV for the inelastic SEY and finally $(E_0-5)-(E_0+5)$ eV for the elastic electrons. However if the incident electron energy is greater than 50 eV, one can use the conventional integral ranges.

Elastic secondary electrons: E'_e, is the energy at which $P'_{1,e}$ (elastic SEY) peaks, W and p_e determine the spectral relationship and $P_{1,e}$ defines the elastic SEY behaviour tending towards infinity.

Inelastic secondary electrons: E_r, is the energy at which the inelastic SEY begins to incrase, $P_{1,r}$ is the inelastic SEY tending towards infinity and r defines the spectral relationship.

True secondary electrons: $E_{ts,\max}$, is the energy at which $\delta_{ts,\max}$ (maximum SEY) occurs at and s determines the true SEY behaviour after $\delta_{ts,\max}$.

The remaining parameters σ_e, e_1, e_2, q, r_1, r_2, t_1, t_2, t_3, t_4 are used to define either the emitted energy spectrum or the angle-dependent SEY relationship for each type of secondary electrons (equations (47) and (48) in Furman's model [45]) and are chosen based on recent measurements of copper taken by CERN. The phenomenological parameters, ϵ_n and p_n, for the true secondaries defining their energy spectrum, are taken from Furman's copper. The fits are obtained through these equations and equation (1), where $\theta = 0$:

$$\delta_e(E_o,\theta) = P_{1,e} + \left(P'_{1,e} - P_{1,e}\right)\, \mathrm{e}^{-\left(\left(E_o - E'_e\right)\,/\,W\right)^{p}{}_e\,/\,p_e} \tag{A1}$$

$$\delta_r(E_o,\theta) = P_{1,r}\,\left[1 - \mathrm{e}^{-(E_o-E_r)^r}\right] \tag{A2}$$

$$\delta_{ts}(E_o,\theta) = \delta_{ts,\max}\,\frac{s\,E_0\,/\,E_{ts,\max}}{s-1+\left(E_0\,/\,E_{ts,\max}\right)^s}. \tag{A3}$$

Appendix B. Samples for model validation

Table 3 includes the information necessary to reproduce the copper samples.

Table 3. Sample parameters—all samples processed in a nitrogen atmosphere to supress *CuO* formation. For D7, Himmerlich *et al* [27] applies a coating which enables investigation of solely geometrical effects on SEY. For DOE set, the displacement away from the focus in mm is denoted in the spot size row.

Sample	***G1***	***G2***	***G3***	***D7***
Wavelength (nm)	532	532	532	532
Spot size (μm)	52	52	52	52
Rep rate (kHz)	200	200	200	200
Pulse width (ps)	10	10	10	10
Power (W)	8	8	8	4
Hatch distance (μm)	91	91	91	45
Pulses per spot	2080	1040	346.667	693
IR1	**IR2**	**DOE1**	**DOE2**	**DOE3**
1030	1030	1030	1030	1030
53	53	81, 0	76, −1.25	81, 0
400	400	400	400	400
0.8	0.8	0.8	0.8	0.8
5.2	5.94	9.65	9.65	6.68
45	45	70	70	90
1060	707	1200	1200	1333

ORCID iD

Amin A Din https://orcid.org/0000-0002-2484-3999

References

[1] Seiler H 1982 Secondary electron emission *Scan. Electron Microsc.* **1982** 3 (available at: https://digitalcommons.usu.edu/electron/vol1982/iss1/3)

[2] Zimmermann F 2013 Electron-cloud effects in past and future machines – walk through 50 years of electron-cloud studies *Conf. Proc. C* **1206051** 9–17

[3] Caspers F, Rumolo G, Zimmermann F and Scandale W 2009 Beam-induced multipactoring and electron-cloud effects in particle accelerators *Int. Workshop in Multipactor, Corona and Passive Intermodulation (MULCOPIM)* pp 24–26

[4] Caspers E, Morvillo M and Ruggiero E 1998 Surface resistance measurements for the LHC beam screen *Proc. IEEE Particle Accelerator Conf.* vol 1 pp 75–77

[5] Cruikshank P *et al* 1997 Mechanical design aspects of the LHC beam screen LHC Project Report 128

[6] Baglin V, Ph L, Tavian L and Van Weelderen R 2013 Cryogenic beam screens for high-energy particle accelerators *24th Int. Cryogenic Engineering Conf.*

[7] Jimenez J M *et al* 2002 Electron Cloud with LHC-type beams in the SPS : a review of three years of measurements *Mini Workshop on Electron Cloud Simulations for Proton and Positron Beams* vol 13

[8] Aberle O *et al* and 2020 High-luminosity Large Hadron Collider (HL-LHC): Technical design report *CERN Yellow Reports: Monographs* (CERN) pp 17–30

[9] Dengra C P, Molina J F and Barcelona A S 2023 New storage and data access solution for CMS experiment in Spain towards HL-LHC era *J. Phys.: Conf. Ser.* 2438

[10] Phys J A 2021 Investigation on secondary electron emission characteristics of double-layer structures investigation on secondary electron emission characteristics of double-layer structures *AIP Publ. LLC* **129** 093304

[11] Zhu X *et al* 2020 Theoretical and experimental investigation of secondary electron emission characteristics of ALD-ZnO conductive films theoretical and experimental investigation of secondary electron emission characteristics of ALD-ZnO conductive films *J. Appl. Phys.* **128** 065102

[12] Zhu X, Guo J, Li X, Zhou R and Wang D 2021 Evolvement investigation of secondary electron emission for Ultrathin MgO coatings prepared by atomic layer deposition *MDPI Appl. Sci.* **11** 4801

[13] Wang D, Cai Y, He Y, Xu Y and Jia Q 2022 Electron emission properties of silver oxide and its impact on the secondary emission yield of air-exposed silver *Results Phys.* **33** 105231

[14] Aguilera L, Montero I, Dávila M E, Ruiz A, Galán L, Nistor V, Raboso D, Palomares J and Soria F 2013 CuO nanowires for inhibiting secondary electron emission *J. Phys. D: Appl. Phys.* **46** 165104

[15] Qiu X, Saed M A, Mankowski J J, Dickens J, Neuber A and Joshi R P 2021 Model evaluations of multipactor suppression in rectangular waveguides through grooved surfaces and static magnetic field *AIP Adv.* **11** 025039

[16] Suharyanto S M, Saito Y, Tumiran Y Y and Kobayashi S 2006 Influence of mechanical finishing on secondary electron emission of alumina ceramics *Proc. - Int. Symp. on Discharges and Electrical Insulation in Vacuum, ISDEIV* vol 1 pp 97–100

[17] Sian B S 2020 Low SEY surfaces for future particle accelerators PhD Thesis

[18] Vallgren C Y *et al* 2011 Amorphous carbon coatings for the mitigation of electron cloud in the CERN Super Proton Synchrotron *Accelerators Beams* **071001** 1–11

[19] He P, Hseuh H C, Todd R, Henrist B, Hilleret N, Le Pimpec F, Kirby R E, Pivi M, Kato S and Nishiwaki M 2004 Secondary electron emission measurements for tin coating on the stainless steel of SNS accumulator ring vacuum chamber *9th European Particle Accelerator Conf. (EPAC 2004)*

[20] Petit V, Taborelli M, Neupert H, Chiggiato P and Belhaj M 2019 Role of the different chemical components in the conditioning process of air exposed copper surfaces *Phys. Rev. Accelerators Beams* **22** 83101

[21] Baglin V, Bojko J, Gröbner O, Henrist B, Hilleret N, Scheuerlein C and Taborelli M 2000 The secondary electron yield of technical materials and its variation with surface treatments Epac 2000

[22] Bajek D *et al* 2020 Role of surface microgeometries on electron escape probability and secondary electron yield of metal surfaces *Sci. Rep.* **10** 1–8

[23] Valizadeh R, Malyshev O B, Wang S, Zolotovskaya S A, Gillespie W A and Abdolvand A 2014 Low secondary electron yield engineered surface for electron cloud mitigation *Appl. Phys. Lett.* **105** 231605

[24] Calatroni S *et al* 2019 Cryogenic surface resistance of copper: investigation of the impact of surface treatments for secondary electron yield reduction *Phys. Rev. Accel. Beams* **22** 63101

[25] Tang G, Hourd A C and Abdolvand A 2012 Nanosecond pulsed laser blackening of copper *Appl. Phys. Lett.* **101** 231902

[26] Yao M-l, Suetsugu Y, Shibata K, Ishibashi T and Hisamatsu H 2022 Suppression of electron cloud using copper thermal spray coating in SuperKEKB *Vacuum* **207** 111619

[27] Himmerlich M *et al* 2023 Efficient combination of surface texturing and functional coating for very low secondary electron yield surfaces and rough nonevaporable getter films *Adv. Mater. Interfaces* **10** 2201671

[28] Salemme S W R, Baglin V, Calatroni S, Chiggiato P, Di Girolamo B, Garcia- Tabares Valdivieso E, Jenninger B, Prever-Loiri L, Sitko M and Abdolvand A 2018 First beam test of laser engineered surface structures (LESS) at cryogenic temperature in CERN SPS accelerator *J. Phys.: Conf. Ser.*

[29] Liu C 2005 A study of particle generation during laser ablation with applications by engineering-mechanical enginnering *PhD Thesis*

[30] Fernández-Arias M B, Val M D and Riveiro J 2020 Fabrication and deposition of copper and copper oxide nanoparticles by laser ablation in open air *Nanomaterials* **10** 1–16

[31] Al-Antaki A H M, Luo X, Duan X, Lamb R N, Hutchison W D, Lawrance W and Raston C L 2019 Continuous flow copper laser ablation synthesis of copper(I and II) oxide nanoparticles in water *ACS Omega* **4** 13577–84

[32] Ariana R 2019 Surface chemistry and composition-induced variation of laser interference-based surface treatment of Al alloys *Appl. Surf. Sci.* **489** 1–23

[33] Reinhardt H, Kroll M, Karstens S L, Schlabach S, Hampp N A and Tallarek U 2020 Nanoscaled fractal superstructures via laser patterning - a versatile route to metallic hierarchical porous materials *Adv. Mater. Interfaces* **8** 2000253

[34] Bez E *et al* 2023 Influence of wavelength and accumulated fluence at picosecond laser-induced surface roughening of copper on secondary electron yield *J. Appl. Phys.* **133** 035303

[35] Smausz T *et al* 2016 Study on the effect of ambient gas on nanostructure formation on metal surfaces during femtosecond laser ablation for fabrication of low-reflective surfaces *Appl. Surf. Sci.* **389** 1113–9

[36] Lorenz P, Himmerlich M, Ehrhardt M, Bez E, Bogdanowicz K, Taborelli M and Zimmer K 2022 Secondary electron yield reduction of copper after 355 nm ultrashort pulse laser ablation *Lasers Manuf. Mater. Process.* **9** 135–50

[37] Bonse J, Höhm S, Kirner S, Rosenfeld A and Krüger J 2016 Laser-induced Periodic Surface Structures (LIPSS) - a scientific evergreen *Optics InfoBase Conf. Papers* vol 23

[38] Taborelli M 2020 Secondary electron yield of surfaces: what we know and what we still need to know *ECLOUD'18: Proc. Joint INFN-CERN-ARIES Workshop on Electron-Cloud Effects*

[39] Pivi M, King F K, Kirby R E, Raubenheimer T O, Stupakov G and Le Pimpec F 2008 Sharp reduction of the secondary electron emission yield from grooved surfaces *J. Appl. Phys.* **104** 104904

[40] Ye M, Wang D and He Y 2017 Mechanism of total electron emission yield reduction using a micro-porous surface *J. Appl. Phys.* **121** 124901

[41] Pierron J *et al* 2018 Effect of rectangular grooves and checkerboard patterns on the electron emission yield *J. Appl. Phys.* **124** 095101

[42] Sattler J M, Coutu R A, Lake R, Laurvick T, Back T and Fairchild S 2017 Modeling micro-porous surfaces for secondary electron emission control to suppress multipactor *J. Appl. Phys.* **122** 055304

[43] Ye M, Feng P, Li Y, Wang D, He Y and Cui W 2019 The total secondary electron yield of a conductive random rough surface *Appl. Phys.* **125**

[44] Wang D, He Y, Ye M, Peng W and Cui W 2017 Secondary electron emission characteristics of nanostructured silver surfaces *J. Appl. Phys.* **122** 153302

[45] Furman M A and Pivi M T 2002 Probabilistic model for the simulation of secondary electron emission *Phys. Rev. Spec. Top. - Accel. Beams* **5** 82–99

[46] Hilleret N, Scheuerlein C and Taborelli M 2003 The secondary-electron yield of air-exposed metal surfaces *Appl. Phys.* **1091** 1085–91

[47] Montero I, Aguilera L, Dávila M E and Nistor V C 2014 Secondary electron emission under electron bombardment from graphene nanoplatelets *Appl. Surf. Sci.* **291** 74–77

[48] Schulte S, Hartung G, Kröger J, Himmerlich M, Petit V and Taborelli M 2020 Energy-resolved secondary-electron emission of candidate beam screen materials for electron cloud mitigation at the Large Hadron Collider *Phys. Rev. Accel. Beams* **23** 103101

[49] Uren R, Din A, Wackerow S, Bez E, Pfeiffer S, Rimoldi M, Himmerlich M, Taborelli M and Abdolvand A 2023 Out of focus ultrafast processing of metals for reduced secondary electron yield *Opt. Mater. Express* **13** 1228–40

[50] Nivas J J *et al* 2021 Secondary electron yield reduction by femtosecond pulse laser-induced periodic surface structuring, Surf. Interfaces **25** 101179

[51] Calatroni S, Garcia-Tabares Valdivieso E, Perez Fontenla A T, Taborelli M, Neupert H, Himmerlich M, Chiggiato P, Bajek D, Wackerow S and Abdolvand A 2020 Optimization of the secondary electron yield of laser-structured copper surfaces at room and cryogenic temperature *Phys. Rev. Accel. Beams* **23** 33101

[52] Pinto P C *et al* 2013 Carbon coatings with low secondary electron yield *Vacuum* **98** 29–36

[53] Hu X-C, Zhang H-B, Cao M, Zhang N and Cui W-Z 2014 Heating-induced variations of secondary electron emission from ion-cleaned copper samples *Micron* **64** 52–56

[54] Barnes M J, Adraktas A, Bregliozzi G, Goddard B, Ducimetière L, Salvant B, Sestak J, Cid L V, Weterings W and Vallgren C Y 2017 Operational experience of the upgraded LHC injection kicker magnets during run 2 and future plans *IPAC 2017 - Proc. 8th Int. Particle Accelerator Conf.* pp 3495–8

[55] Ludwick J, Iqbal A, Gortat D, Cook J D, Cahay M, Zhang P, Back T C, Fairchild S, Sparkes M and O'Neill W 2020 Angular dependence of secondary electron yield from microporous gold surfaces *J. Vacuum Sci. Technol.* B **38** 054001

[56] Fil N 2017 Caractérisation et modélisation des propriétés d'émissionélectronique sous champ magnétique pour des systèmes RF hautes puissances sujetsà l'effet multipactor. *PhD Thesis*

[57] Cimino R, Angelucci M, Gonzalez L A and Larciprete R 2020 SEY and low-energy SEY of conductive surfaces *J. Electron Spectrosc. Relat. Phenom.* **241** 146876